

Transmission Line and Equivalent Circuit Models for Plasmonic Waveguide Components

Şükrü Ekin Kocabaş, *Student Member, IEEE*, Georgios Veronis, *Member, IEEE*, David A. B. Miller, *Fellow, IEEE*, and Shanhui Fan, *Senior Member, IEEE*

Abstract—Modeling of waveguide junctions using transmission lines and lumped circuit elements is common practice in microwave networks. By the help of the scattering matrix formalism, it is possible to describe junction effects in a very concise way. Such a representation is crucial for the design of complex systems containing many interacting parts. Using scattering matrices, we characterize symmetric junctions between 2-D metal–insulator–metal (MIM) waveguides with optical signals at infrared frequencies (1550 nm) propagating in them. We verify our characterization by perfectly matching a wavelength-sized MIM waveguide to a subwavelength-sized one using a Smith chart. We then map the scattering matrix description to an equivalent lumped circuit representation and discuss the physical significance of its elements. We show that the simplified characteristic impedance model is appropriate for the deep subwavelength regime. The scattering matrix model for the MIM junctions leads to simplified analysis that can be integrated into circuit modeling software packages, such as SPICE.

Index Terms—Equivalent circuits, optical waveguides, parallel plate waveguides, plasmons, scattering matrices, waveguide discontinuities, waveguide junctions.

I. INTRODUCTION

MODELING electromagnetic wave propagation using transmission lines has been one of the most important achievements of microwave network theory [1]. The concept of impedance [2] and understanding the effects of waveguide discontinuities in terms of lumped circuit elements were crucial in this respect.

Recent interest in the use of metals to design optical components opened up the possibility of guiding light in subwavelength structures. The optical properties of metals at infrared and visible wavelengths enable these designs. It is hoped that the size mismatch between modern electronic components with critical dimensions on the order of tens of nanometers and the micrometer-scaled optical devices will be bridged by the use

Manuscript received December 3, 2007; revised February 28, 2008. This work was supported in part by the Air Force Office of Scientific Research (AFOSR) Chip Scale Surface Plasmon Enabled Nano Structures Multidisciplinary University Research Initiatives (MURI), in part by the Focus Center Research Program/Defense Advanced Research Projects Agency (FCRP/DARPA) Interconnect Focus Research Center, and in part by the DARPA Microsystems Technology Office (MTO).

Ş. E. Kocabaş, D. A. B. Miller, and S. Fan are with Ginzton Laboratory, Stanford University, Stanford, CA 94305-4088, USA (e-mail: kocabas@ieee.org; dabm@ee.stanford.edu; shanhui@stanford.edu).

G. Veronis was with Ginzton Laboratory, Stanford University, Stanford, CA 94305-4088, USA. He is now with the Department of Electrical and Computer Engineering and the Center for Computation and Technology, Louisiana State University, Baton Rouge, LA 70803, USA (e-mail: gveronis@lsu.edu).

Color versions of one or more of the figures in this paper are available online at <http://ieeexplore.ieee.org>.

Digital Object Identifier 10.1109/JSTQE.2008.924431

of nanometallic structures [3]. Even though the properties of metals are quite different at optical wavelengths compared to the microwave, designs that are qualitatively similar to their low-frequency counterparts have been demonstrated at optical frequencies [4]. It is intriguing to ask whether methods of microwave can be applied to this new generation of nanometallic structures to come up with concise descriptions of components that can lead to a simplified approach to the design of functional systems composed of many interacting parts.

Transmission lines and lumped element circuit descriptions have been shown to be useful concepts for optical components [5]–[10]. In this paper, we will focus on the 2-D *metal–insulator–metal* (MIM) waveguide (here we will use this term “MIM” to apply only to waveguides at optical or infrared frequencies, as distinct from “parallel plate” waveguides, which are mechanically similar structures but used in the microwave or radio frequency regime). MIM waveguides have been extensively studied [11]–[13] in the literature. It has also been shown that the main TM mode of an MIM waveguide continuously changes to that of the TEM mode of a parallel-plate waveguide with *perfect electric conductor* (PEC) boundaries as the frequency of operation is decreased [14]. Our study will investigate the symmetric junctions of MIM waveguides. It is possible to find examples of analysis for various junction geometries including MIM waveguide to free space [15], one MIM waveguide to two MIM waveguides [16], MIM waveguide bends [5], [17], dielectric slab waveguide to MIM waveguide [18], PEC parallel-plate waveguide to PEC parallel-plate waveguide [19], surface plasmon to surface plasmon [20], [21], and MIM waveguide to MIM waveguide [22]. In [23], junctions made by microgratings on metallic wires are modeled as Bragg mirrors. The numerical methods of analysis for nanometallic structures are reviewed in [24].

In this paper, in Section II, we will characterize the modal reflection and transmission from MIM junctions using the scattering matrix approach, a commonly used method in microwave network theory. Then, in Section III, to test our characterization, we will design a cascade connection of MIM junctions to couple the mode of a wavelength-sized MIM waveguide to that of a subwavelength one with zero reflection. Lastly, in Section IV, we will represent the scattering matrix of MIM junctions in terms of an equivalent lumped circuit model and discuss the physical significance of its elements. Throughout our analysis, we will compare MIM waveguides to PEC parallel-plate waveguides and comment on the similarities and the differences between the two. We will draw our conclusions in Section V.

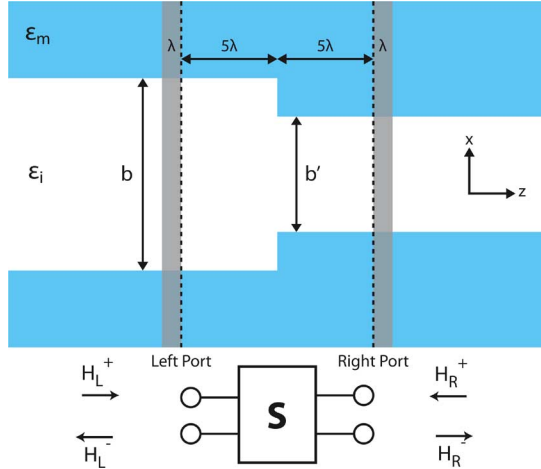


Fig. 1. Description of the modeling geometry. Dashed lines represent the location of the left and right ports of the overall scattering matrix \mathbf{S} that describes this junction (schematically shown in the bottom). Gray areas on the left and right of the ports are the regions in the simulation space used to extract the reflection coefficients S_{11} and S_{22} .

II. SCATTERING MATRIX DESCRIPTION OF JUNCTIONS

In this section, we will focus on the geometry as shown in Fig. 1. We are considering MIM waveguides, consisting of two layers of metal separated by an insulating dielectric layer. The metals are presumed to be thick in the vertical (x) direction in Fig. 1, and to extend arbitrarily far in the directions in and out of the page. We are considering the modes of propagation in the horizontal (z) directions. We are particularly interested in what happens at the symmetric interfaces between two (or more) such MIM waveguides with different dielectric thicknesses. Fig. 1 shows the interface between two such guides. The variable b will denote the insulator thickness for the left waveguide and b' will be used for right waveguide's insulator thickness. We will assume that the insulating region is free space with a permittivity $\epsilon_i = 1$. For our simulations, the metal is silver with a permittivity of $\epsilon_m = -143.497 - i9.517$ [25], [26], though similar general results are expected for other metals such as aluminum or gold. We will use $e^{+i\omega t}$ for the time dependence of electromagnetic fields where ω is the angular frequency. The wavelength of operation is fixed at $\lambda = 1550$ nm, in the L-band of optical telecommunications. The main mode of the system is an even TM mode (here, by TM we mean that the magnetic field H_y is in the direction out of the plane of the paper in Fig. 1). Due to the symmetry of the junction, only even TM modes can be excited using an incident wave, which itself is a TM wave that is an even function with respect to the center of the guide. We therefore have only three field components: H_y , E_x , and E_z .

Using the dispersion equation for even modes of the MIM waveguide [13], it can be shown that only a single even propagating mode can exist for $b < 0.97\lambda$ for our choice of ϵ_m , ϵ_i , and λ . The condition for the PEC parallel-plate waveguide is similar, where only a single even propagation mode exists for $b < 1.0\lambda$. When there is only one propagating mode, far away from the waveguide junction, the fields can be written in terms of that main mode of the system since all higher order modes will

have an exponential decay much faster compared to the main propagating mode. Under such circumstances, the effects of the waveguide junction on the propagating modes can be described using the single-mode *scattering matrix* (\mathbf{S}) formalism [27]. In the terminology of the scattering matrix, the forward and backward mode amplitudes are considered to scatter from one “port” to another. Here, we can think of the ports as being the left and right port planes shown in Fig. 1. These ports are sufficiently far to the left and right of the junction that the fields have settled down again to being the propagating modes of the guides (nearer to the interface, there will in general be other field behavior, including various near-field components that decay rapidly with distance).

If we can deduce the scattering matrix for such a junction, then we can have a very simple way of modeling the behavior of structures containing such junctions, as is already well known in the modeling of microwave guides. The elements of the scattering matrix S_{11} , S_{12} , S_{21} , and S_{22} are complex numbers that describe the phase and magnitude of the reflection and transmission of the main modes. Thus, in general, there are eight independent real numbers in \mathbf{S} . However, under certain conditions the number of independent parameters can be reduced. First of all, if the system is composed of reciprocal media (i.e., symmetric permittivity and permeability tensors), then, by using the Lorentz reciprocity theorem, it can be shown that $S_{12} = S_{21}$. Note that this equality implies a certain normalization of the modes [27, eq. (5.11) and (5.40)], specifically

$$\oint_{\mathbf{A}} \mathbf{E}_L \times \mathbf{H}_L \cdot d\mathbf{A} = \oint_{\mathbf{A}} \mathbf{E}_R \times \mathbf{H}_R \cdot d\mathbf{A} = 1 \quad (1)$$

where $\mathbf{E}_{\{L,R\}}$ and $\mathbf{H}_{\{L,R\}}$ denote the electric (\mathbf{E}) and magnetic (\mathbf{H}) components of the main propagating modes on the left (L) and the right (R) of the waveguide junction. \mathbf{A} is the cross section of the waveguides perpendicular to the direction of propagation. Also note that for lossless systems, \mathbf{S} is a unitary matrix [27] (though in general, in this paper, we will be considering systems with loss). As a result, using reciprocity it is possible to describe a lossy junction using six real numbers, two for each of S_{11} , S_{12} , and S_{22} . When there is no loss, we only need three real numbers due to the unitarity of \mathbf{S} .

The scattering matrix description based on the propagation of the modes can be mapped to an equivalent transmission line with propagating voltage and current waves. The voltage V on the transmission line is defined as proportional to the transverse electric field of the mode and the current I is defined as proportional to the transverse magnetic field. The first condition on the proportionality factors is that the average power is given by $\text{Re}(VI^*/2)$ as in a circuit. The second condition on the proportionality factors is that V/I of an incident wave on the transmission line should be the characteristic impedance of the mode [28, p. 532]. We know that no unique definition of the characteristic impedance can be made for non-TEM modes as shown in [29, p. 66] and [30, pp. 226–228]. However, the normalization condition (1) on the modes, which gives us symmetric scattering matrices, automatically leads to transmission lines with characteristic impedance of unity, independent of the

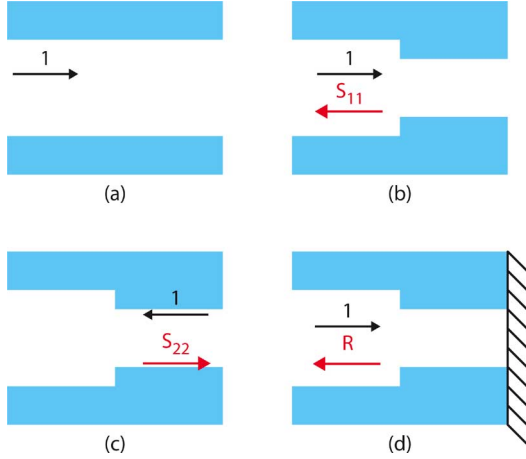


Fig. 2. Description of the steps taken in extracting \mathbf{S} from fields. (a) Calibration simulations with uniform insulator widths of b and b' , which give the wave vector k and the values of the incoming fields at the left, $H_L^+ \Psi_L(x)$, and right ports, $H_R^+ \Psi_R(x)$. (b) Field impinging from the left side, which leads to S_{11} . (c) Field impinging from the right side, which leads to S_{22} . (d) Simulation domain is terminated by a perfect electric conductor at the right input port plane. S_{12} is extracted from the reflection coefficient R using the previously calculated S_{11} and S_{22} .

modal properties. A discussion and proof of this point is given in [27], [31, pp. 186–188], and [32, p. 171].

After that brief introduction to the theory of scattering matrices, now we will describe the method we used to extract the elements of \mathbf{S} from the electromagnetic fields in such waveguide junctions. We solved Maxwell's equations using the *finite-difference frequency-domain* (FDFD) method [5]. In the vicinity of the waveguide junction, higher order modes will be excited. We initially chose the left and right ports of our junction sufficiently (5λ) away from the physical junction, where the amplitudes of the higher order modes are negligible. In the following, we will formulate \mathbf{S} in terms of the TM field component H_y . We will use $\Psi_L(x)$ to denote the main mode of the left waveguide and $\Psi_R(x)$ for the right waveguide.

The scattering matrix relates the amplitudes and phases of the modes that arrive at the left and right ports, H_L^+ , H_R^+ to the amplitudes and phases of the modes that propagate away from the ports, H_L^- and H_R^- . Formally we can write

$$\begin{pmatrix} H_L^- \\ H_R^- \end{pmatrix} = \begin{pmatrix} S_{11} & S_{12} \\ S_{21} & S_{22} \end{pmatrix} \begin{pmatrix} H_L^+ \\ H_R^+ \end{pmatrix} \quad (2)$$

In order to extract \mathbf{S} , we need to know the fields that arrive at the left and right ports from our numerical sources in the simulation domain. To do that, we perform two calibration simulations (one for the left waveguide, another for the right waveguide) without any discontinuities, as shown in Fig. 2(a), and record the fields. This gives us the required $H_{\{L,R\}}^+ \Psi_{\{L,R\}}(x)$ in addition to the propagation vectors $k_{\{L,R\}}$ of the two main modes for guides of insulator thicknesses b and b' , respectively. Then, we perform two more simulations where we send the mode from the left and from the right waveguide to the discontinuity, as schematically shown in Fig. 2(b) and (c). From the results of the simulation in Fig. 2(b), for the fields to the left of the left port $H_L(x, z)$ we

get

$$\begin{aligned} H_L(x, z) &= [H_L^+ e^{-ik_L z} + H_L^- e^{+ik_L z}] \Psi_L(x) \\ &= [H_L^+ (e^{-ik_L z} + S_{11} e^{+ik_L z})] \Psi_L(x) \end{aligned}$$

where the location of the left port determines the origin for z and in (2) we used the fact that $H_R^+ = 0$ for the simulation depicted in Fig. 2(b). Simple algebra gives

$$S_{11} = \frac{H_L(x, z)}{H_L^+ \Psi_L(x)} e^{-ik_L z} - e^{-2ik_L z} \quad (3)$$

Ideally, S_{11} should be independent of the coordinates x and z . However, due to finite reflections from the perfectly matched layers (PMLs) at the boundaries of our simulation domain, we do get some small variations in S_{11} . To mitigate these effects, we extract the complex valued S_{11} at various locations in our simulation domain shown with the gray area on the left of the junction in Fig. 1, and average the results. Very similarly, we also extract S_{22} from the results of the simulation of Fig. 2(c).

In order to extract S_{12} , we terminate our simulation domain at the plane of the right port with a perfect electric conductor. Such a termination results in zero tangential electric fields, and therefore, gives -1 for the reflection coefficient of the transverse electric field E_x and $+1$ for the magnetic field H_y . Thus, at the right port, we get $H_R^- = H_R^+$. Using this equality in (2) gives

$$\begin{pmatrix} H_L^- \\ H_R^- \end{pmatrix} = \begin{pmatrix} S_{11} & S_{12} \\ S_{21} & S_{22} \end{pmatrix} \begin{pmatrix} H_L^+ \\ H_R^+ \end{pmatrix}. \quad (4)$$

We call the reflection coefficient from the junction in Fig. 2(d), R . We extract R using the same method as we used in the extraction of S_{11} . From the definition

$$R = \frac{H_L^-}{H_L^+}$$

and using (4) one gets

$$R = S_{11} + \frac{S_{12} S_{21}}{1 - S_{22}} = S_{11} + \frac{S_{12}^2}{1 - S_{22}} \quad (5)$$

where, in the last equality, we used the fact that $S_{21} = S_{12}$. From the knowledge of R , S_{11} , and S_{22} one can easily invert (5) to calculate S_{12} .

After we calculate \mathbf{S} for the ports defined in Fig. 1, we shift both the left and right reference planes back to the exact location of the junction using

$$\mathbf{S}_J = \begin{pmatrix} e^{ik_L \ell_L} & 0 \\ 0 & e^{ik_R \ell_R} \end{pmatrix} \mathbf{S} \begin{pmatrix} e^{ik_L \ell_L} & 0 \\ 0 & e^{ik_R \ell_R} \end{pmatrix} \quad (6)$$

where $\ell_L = \ell_R = 5\lambda$, as defined in Fig. 1, and \mathbf{S}_J is the effective scattering matrix for the case where the left and right ports are projected back to coincide with the junction plane [27]. For the sake of notational abbreviation, from this point on, we will use \mathbf{S} to imply \mathbf{S}_J . Note that this effective scattering matrix is defined just for the algebraic convenience of having a scattering matrix associated directly with the position of the interface. In fact, the fields near the interface are not describable by these single main modes because of various near-field effects of higher order modes.

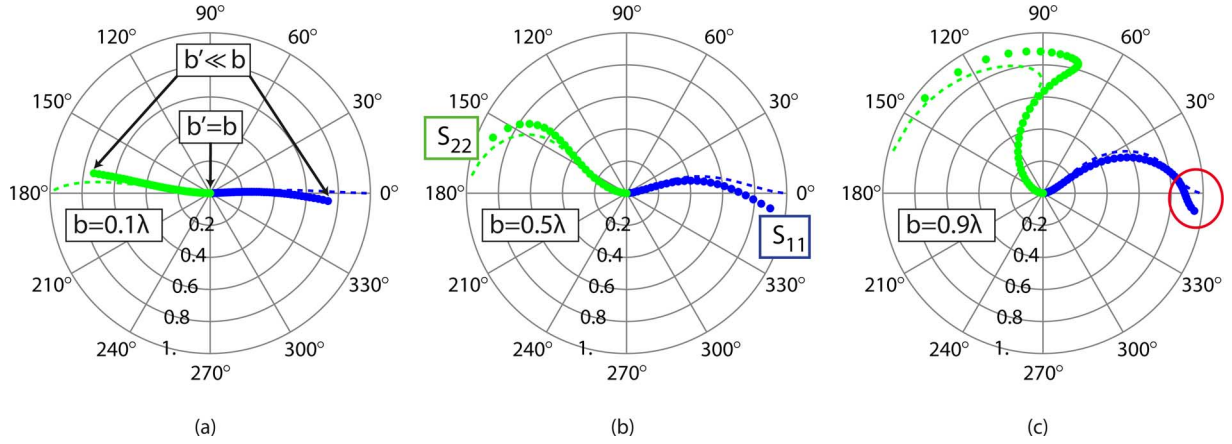


Fig. 3. Polar plot of S_{11} (•, plots heading out to the right half of the diagram) and S_{22} (•, plots heading out toward the left half of the diagram) on the complex plane, which is called the Smith chart in the microwave literature. Circles are used for the MIM case, dashed lines are used for the PEC case. Each subplot is for a fixed left waveguide thickness b with a varying right waveguide thickness b' . In all three subplots, the origin is the zero reflection point that corresponds to $b' = b$. As b' decreases progressively toward zero, we move progressively along the curves away from the origin. The end points of the dashed curves on the unit circle correspond to $b' = 0$. In all three cases, the wavelength of light is fixed at $\lambda = 1550$ nm. (a) $b = 0.1\lambda$. (b) $b = 0.5\lambda$. (c) $b = 0.9\lambda$.

We fixed the frequency of operation at $\lambda = 1550$ nm and calculated \mathbf{S} for various right waveguide thicknesses (b') while keeping the width of the left waveguide (b) constant. In Fig. 3, three sets of results are shown for $b = \{0.1\lambda, 0.5\lambda, 0.9\lambda\}$. The outermost circle in the plots is the unit circle in the complex plane, and the real and imaginary parts of the reflection coefficients are plotted for different $\{b, b'\}$ pairs. We also plotted S_{11} and S_{22} as a function of b' for the PEC case using the well-known mode-matching technique [33] for the same set of b . We verified our mode-matching approach by FDFD that gave the same results. The reason we did mode-matching calculations was to verify the PEC parallel-plate waveguide results in the literature, as well as to check our numerical extraction of \mathbf{S} in a numerically independent manner. Making the metals perfect turns the MIM waveguide into the PEC parallel-plate waveguide. It can be seen that the shapes of curves for the PEC parallel-plate and MIM waveguides are qualitatively similar. Also note that the polar plot of the reflection coefficients is nothing other than the Smith chart of the microwave theory [34, p. 48], which we will use in the next section.

III. CASCADE CONNECTION OF JUNCTIONS

Now that we have a methodology to characterize MIM junctions, in this section, we will test the utility of the scattering matrix description by numerically simulating mode propagation through a cascade connection of junctions and comparing the results with the predictions of the scattering matrix formalism. First, let us define the building blocks that will be used throughout this section.

When different scattering matrices are cascaded, the overall scattering matrix for the system is not the product of the individual scattering matrices. For cascade connections, the *transfer matrix* \mathbf{T} leads to a much simpler formulation [32, pp. 181–182]. \mathbf{S} has $\{H_L^+, H_R^+\}$ and $\{H_L^-, H_R^-\}$ as an input–output pair, whereas \mathbf{T} has $\{H_R^-, H_R^+\}$ and $\{H_L^-, H_L^+\}$, respectively. Given one representation, one can easily compute the other through

simple algebraic manipulations.

$$\begin{pmatrix} H_L^+ \\ H_L^- \end{pmatrix} = \begin{pmatrix} T_{11} & T_{12} \\ T_{21} & T_{22} \end{pmatrix} \begin{pmatrix} H_R^- \\ H_R^+ \end{pmatrix}$$

$$T_{11} = \frac{1}{S_{21}} \quad T_{12} = -\frac{S_{22}}{S_{21}} \quad (7)$$

$$T_{21} = \frac{S_{11}}{S_{21}} \quad T_{22} = S_{12} - \frac{S_{11}S_{22}}{S_{21}}.$$

In order to have $H_L^- = 0$, one should have $T_{21}H_R^- + T_{22}H_R^+ = 0$, which can be cast in terms of the scattering parameters using (7) as

$$S_{11}H_R^- = (S_{11}S_{22} - S_{12}S_{21})H_R^+. \quad (8)$$

A. Conditions for Zero Reflection

1) *Lossy Case*: Let us investigate the case when two junctions characterized by two different scattering matrices, ${}^L\mathbf{S}$ and ${}^R\mathbf{S}$, are separated by a center waveguide of length ℓ , as shown in Fig. 4(a). Suppose that we adjust our excitation amplitude such that the mode that propagates toward the right junction at its input plane, which is the junction plane, has unit strength. That choice of normalization leads to $H_C^- = e^{ik_C\ell}$ and $H_C^+ = {}^R S_{11}e^{-ik_C\ell}$, where k_C is the wave vector of the center waveguide. With these definitions, the condition for zero reflection, (8), for the left junction can be written as

$${}^L S_{11}H_C^- = ({}^L S_{11} {}^L S_{22} - {}^L S_{12} {}^L S_{21})H_C^+$$

$${}^L S_{11}e^{ik_C\ell} = ({}^L S_{11} {}^L S_{22} - {}^L S_{12} {}^L S_{21}){}^R S_{11}e^{-ik_C\ell}$$

$$e^{-2ik_C\ell} = \frac{{}^L S_{11}/{}^R S_{11}}{{}^L S_{11} {}^L S_{22} - {}^L S_{12} {}^L S_{21}}.$$

Now, let us simplify this equality. For reciprocal media, $S_{12} = S_{21}$, we can write

$$e^{-2ik_C\ell} = \frac{{}^L S_{11}/{}^R S_{11}}{{}^L S_{11} {}^L S_{22} - {}^L S_{21}^2}. \quad (9)$$

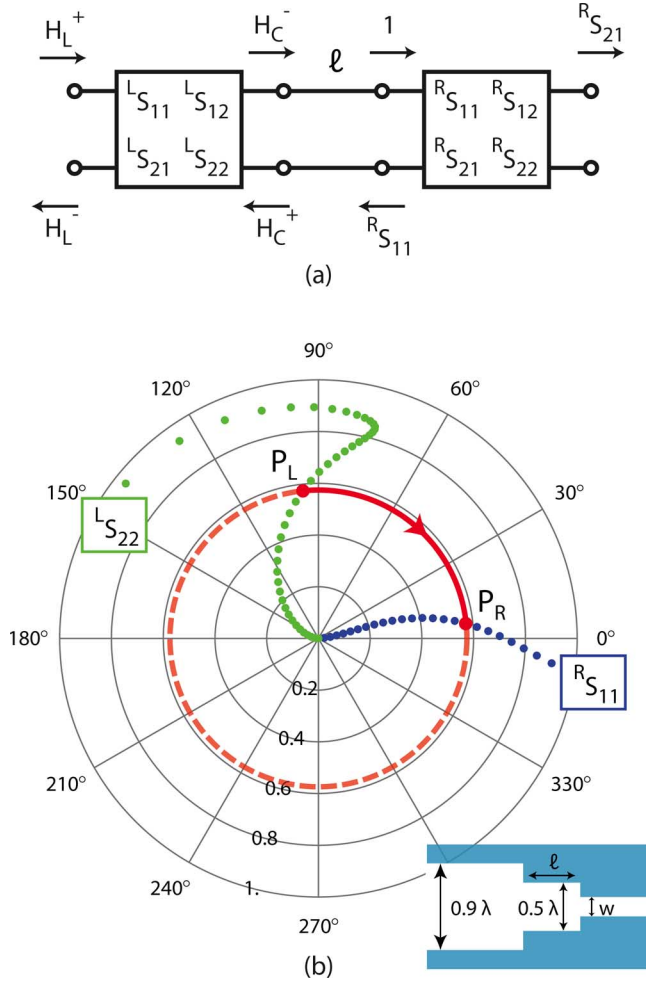


Fig. 4. (a) Schematic diagram of modal propagation. The left and right junctions are shown as boxes with an \mathbf{S} matrix description. The center waveguide is shown as a transmission line of length ℓ . The source that creates the fields is normalized such that the mode that propagates to the right has a unit magnitude at the input of the right junction. (b) Graphical solution of (11) and (12) on the complex plane. Point P_L is the location of the left junction on the $L_{S_{22}}$ curve where $b = 0.9\lambda$ and $b' = 0.5\lambda$. Point P_R is the location of the right junction on the $R_{S_{11}}$ curve where $b = 0.5\lambda$ and $b' = 0.16\lambda$.

2) *Lossless Case*: If the system is lossless, then the scattering matrix should be unitary ($\mathbf{S}\mathbf{S}^\dagger = \mathbf{1}$), which implies the following three conditions

$$\begin{aligned} |S_{11}|^2 &= |S_{22}|^2 = 1 - |S_{12}|^2 \\ \frac{S_{12}}{S_{21}^*} &= -\frac{S_{22}}{S_{11}^*} \end{aligned} \quad (10)$$

Using (9) and (10) after some algebra, the zero reflection condition becomes

$$|L_{S_{22}}| = |R_{S_{11}}| \quad (\text{magnitude condition}) \quad (11)$$

$$\angle L_{S_{22}} + \angle R_{S_{11}} = 2k_C\ell + 2\pi n \quad (\text{phase condition}) \quad (12)$$

where n is any integer value, superscripts R and L denote right and left, respectively. “ \angle ” is used to represent the argument of a complex number. What this means is that to match a left waveguide to a right waveguide, one should choose a center waveguide width that satisfies the magnitude condition, and

decide on the length of the center waveguide based on the phase condition.

As a corollary, suppose that the left and right waveguides are the same and are on the order of a wavelength in dimension. Further suppose that the center waveguide has a deep subwavelength size, i.e., it has an insulator width much smaller than the wavelength and the surrounding left and right waveguides’ insulator widths. Due to the symmetry of the system, the magnitude condition is automatically satisfied. One only needs to choose a specific length for the center section to do the matching. Such a geometry can be interesting for sensing applications, where interaction with strongly concentrated fields is desired. Similar observations were made in the language of Fabry–Perot resonances for the limiting case when the right and left waveguides’ insulator thicknesses go to infinity [15].

Once a matching left, center, and right waveguide triplet is found, the procedure can be recursively repeated to cascade more junctions without getting any reflection at the leftmost waveguide.

B. Mode Converter Design

Now that we have the conditions (9), (11), and (12) for zero reflection, we can test their validity. Condition (9) is more general and is applicable to the lossy case. We did a series of simulations in which we extracted \mathbf{S} for a hypothetical lossless metal with a real, negative permittivity $\epsilon_m = -143.497$. The results were very similar to the case in Fig. 3 where the loss was included. That led us to suspect that the conditions for the lossless reciprocal junctions (11) and (12) would be essentially sufficient in the design of a mode converter that converts the mode of a wavelength-sized MIM waveguide ($b = 0.9\lambda$) to that of a subwavelength one with no reflection.

In our design, we choose the left waveguide width to be 0.9λ and the center waveguide width to be 0.5λ , as shown in the inset in Fig. 4(b). The parameters that we need are the insulator width of the right waveguide w and the length of the center waveguide ℓ .

The width of the right waveguide can be chosen by satisfying (11). In Fig. 4(b), P_L is the location of the $b = 0.9\lambda$ to $b' = 0.5\lambda$ junction on the $L_{S_{22}}$ curve. To satisfy (11), we need to have $|L_{S_{22}}| = |R_{S_{11}}|$. The solution can be graphically found by drawing a circle in the complex plane with a radius $|P_L|$ centered at the origin and finding its intersection with the $R_{S_{11}}$ curve. The intersection point is denoted by P_R . P_R corresponds to a right waveguide thickness of 0.16λ . The phase condition (12) is then easily calculated from the phases of the scattering coefficients, $\angle P_L$ and $\angle P_R$. After some simplification through the use of the numerical value for k_C , one gets $\ell/\lambda = 0.1377 + 0.4861n$, where n is any positive integer.

To check our design, we numerically simulated the structure shown in the inset of Fig. 5 using FDFD and looked at the amount of power reflected back as a function of the center waveguide length ℓ . We also calculated the power reflection coefficient through the use of the transfer matrix formalism in which we multiplied the transfer matrices for the right junction \mathbf{T}_R , a center waveguide of length ℓ , \mathbf{T}_C , and the left junction \mathbf{T}_L ,

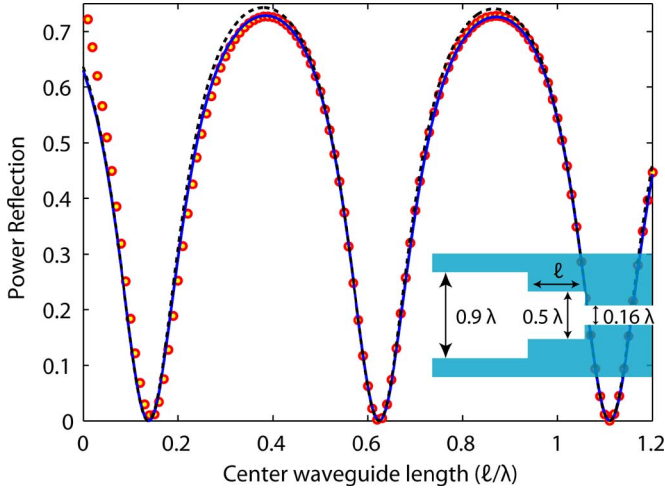


Fig. 5. Test of the scattering matrix description. Horizontal axis is the length of the center waveguide normalized to λ . Vertical axis is the power reflection coefficient. FDFD simulation results (\bullet), transfer matrix calculations using lossy junctions (solid line) and lossless junctions (dashed line) are also plotted. Transfer matrix calculations do take into account the loss in the center waveguide for both cases. As the junctions get very close to each other ($< 0.1\lambda$), transfer matrix model begins to break down due to higher order modal interactions.

to get the overall transfer matrix $\mathbf{T} = \mathbf{T}_L \mathbf{T}_C \mathbf{T}_R$, and plotted $|T_{21}/T_{11}|^2$ of \mathbf{T} as a function of ℓ/λ . We did the calculations for two different sets of $\{\mathbf{T}_R, \mathbf{T}_L\}$: one in which we used the scattering matrices for the lossy junctions and another for the lossless junctions. The center waveguide of length ℓ had loss in both cases, i.e., $k_C = (1.03 - i9.45 \times 10^{-4})2\pi/\lambda$.

Fig. 5 verifies that lossless junction models are quite effective at modeling the waveguide discontinuities and the prediction of the length of the center guide for zero reflection reached by their use, $\ell/\lambda = 0.1377 + 0.4861n$ is very accurate. The lossy junction model on the other hand gives results essentially indistinguishable from the simulation results as long as the two junctions are not very close to each other ($< 0.1\lambda$). When the junctions get very close, the coupling of higher order nonpropagating modes becomes important, and the single-mode modeling we employed in the construction of scattering matrices breaks down. For such closely spaced junctions, the whole structure should be treated as a single unit and its characteristics should be extracted by the techniques described in Section II.

Last, (11) and (12) reproduce the well-known quarter wave ($\lambda/4$) impedance matching formula used at RF [32, Sec. 5.6] where one uses

$$\begin{aligned} -^L S_{11} = {}^L S_{22} &= \frac{(Z_{0C} - Z_{0L})}{(Z_{0C} + Z_{0L})} \\ -^R S_{11} = {}^R S_{22} &= \frac{(Z_{0R} - Z_{0C})}{(Z_{0R} + Z_{0C})} \end{aligned} \quad (13)$$

In this equation, $Z_{0\{L,C,R\}}$ denotes the characteristic impedance of the left, center, and right RF transmission line. Solution of (11) and (12) with (13) and either the condition $Z_{0R} > Z_{0C} > Z_{0L}$

or $Z_{0R} < Z_{0C} < Z_{0L}$ gives

$$Z_{0C} = \sqrt{Z_{0L} Z_{0R}} \quad \text{and} \quad \ell = \frac{\lambda}{4} + n \frac{\lambda}{2} \quad (14)$$

where n is any positive integer. Recently, a power transmission of 86% for a waveguide converter designed using (14) was demonstrated [22].

IV. CIRCUIT MODEL FOR THE WAVEGUIDE JUNCTION

So far, we have characterized the MIM junctions, and with that characterization, designed a waveguide matching section by the use of the scattering matrices. Another important approach in microwave waveguide modeling is the use of equivalent circuit models, which can give an intuitive picture of the system as well as allowing the use of circuit simulators for design.

Here, we relate the scattering matrix and circuit models, and show simplified circuit models that can characterize the MIM waveguide interfaces. Since we only have single propagating modes in the guides we consider, we can also use equivalent transmission lines to describe the propagation between interfaces. Taking these circuit and transmission line approaches together, we can then model a broad range of MIM systems in circuit models.

There is no unique way to describe \mathbf{S} using lumped-circuit elements [35, p. 316]. To choose one circuit out of the infinite possible set that could correspond to the same \mathbf{S} , we will first look at the well-studied PEC case. After reproducing the PEC results, we will then add another term to the PEC parallel-plate waveguide model to account for the properties of metals at optical frequencies. We will compare the lumped-circuit representation with the characteristic impedance models in the literature. At the end of the section, we will justify our choice of the additional circuit element, while we give a physical explanation for the circuit.

A. Exact Model

We will begin our analysis with the PEC case. The solution to the scattering problem for the junction of two PEC parallel-plate waveguides was developed and experimentally verified [36]. It consists of a capacitor with susceptance B and a transformer with a turns ratio of $n : 1$. The susceptance and the turns ratio are described in terms of the geometry of the junction. The susceptance value is given by

$$\begin{aligned} B = \frac{2b}{\lambda} \left\{ \log \left[\left(\frac{1 - \alpha^2}{4\alpha} \right) \left(\frac{1 + \alpha}{1 - \alpha} \right)^{[\alpha + (1/\alpha)]/2} \right] \right. \\ \left. + \left(2 \frac{A + A' + 2C}{AA' - C^2} \right) \right. \\ \left. + \left(\frac{b}{4\lambda} \right)^2 \left(\frac{1 - \alpha}{1 + \alpha} \right)^{4\alpha} \left(\frac{5\alpha^2 - 1}{1 - \alpha^2} + \frac{4\alpha^2 C}{3A} \right)^2 \right\} \end{aligned} \quad (15)$$

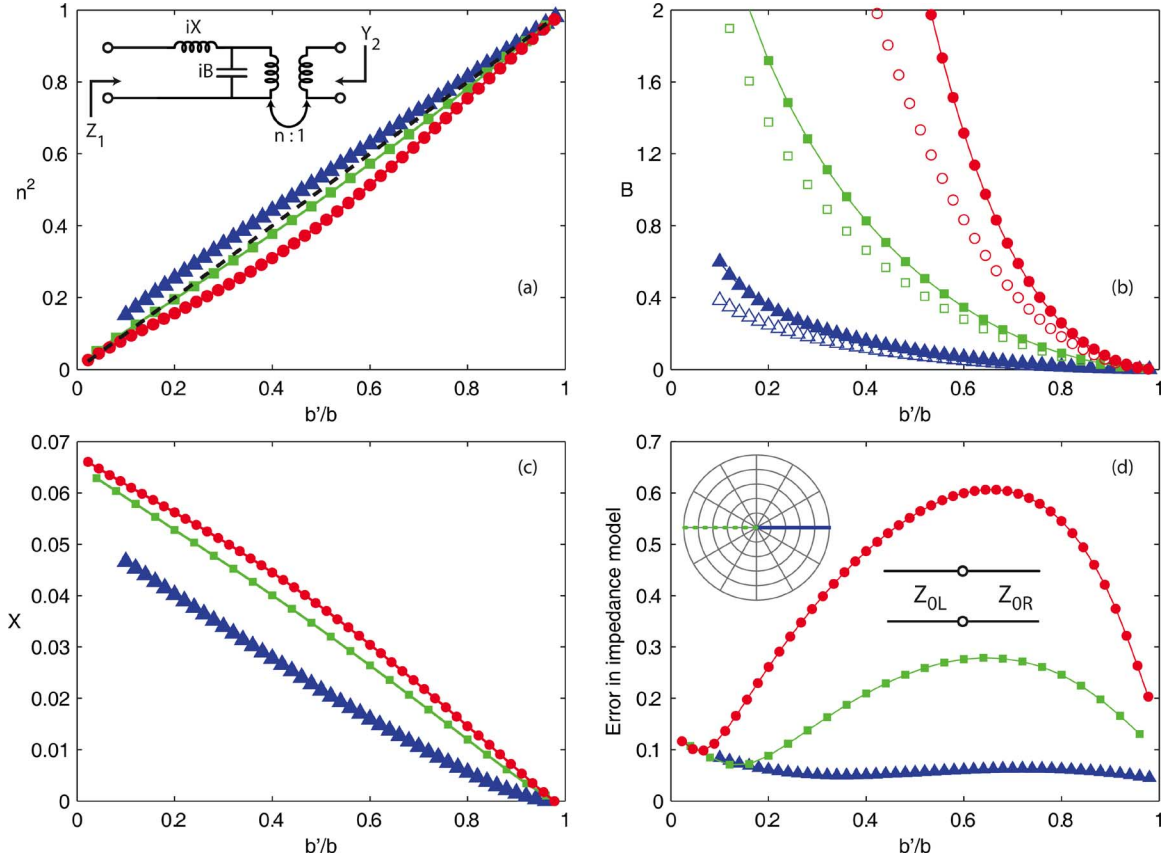


Fig. 6. Circuit description of the lossless ($\epsilon_m = -143.497$) waveguide junction for $b = 0.1\lambda$ (\blacktriangle), $b = 0.5\lambda$ (\blacksquare), $b = 0.9\lambda$ (\bullet). (a) Square of the turns ratio n^2 , which is equivalent to the impedance ratio at the terminals of the transformer. Dashed line is the PEC result described by (16). Inset shows the circuit diagram. (b) Susceptance B for the MIM (\blacktriangle , \blacksquare , \bullet) and the PEC (\triangle , \square , \circ) case. B for the PEC case plotted by the use of (15). (c) Reactance X of the MIM waveguide. $X = 0$ for the PEC parallel plate waveguide. (d) Error in S_{11} defined as $|(S_{11} - S'_{11})/S_{11}|$ where S_{11} is the exact solution, $-S'_{11} = (Z_{0R} - Z_{0L})/(Z_{0R} + Z_{0L})$ is the characteristic impedance model approximation. The inset shows the implication of the characteristic impedance model on the Smith chart where S_{11} (solid line in the inset) and S_{22} (dashed line in the inset) have a π phase shift. Compare with Fig. 3. The error is around 5 percent for $b = 0.1\lambda$ where the π phase shift condition is approximately satisfied. As the dimensions increase, so does the error.

where $\alpha = b'/b$ and

$$A = \left(\frac{1+\alpha}{1-\alpha}\right)^{2\alpha} \frac{1 + \sqrt{1 - (b/\lambda)^2}}{1 - \sqrt{1 - (b/\lambda)^2}} - \frac{1 + 3\alpha^2}{1 - \alpha^2}$$

$$A' = \left(\frac{1+\alpha}{1-\alpha}\right)^{2/\alpha} \frac{1 + \sqrt{1 - (b'/\lambda)^2}}{1 - \sqrt{1 - (b'/\lambda)^2}} + \frac{3 + \alpha^2}{1 - \alpha^2}$$

$$C = \left(\frac{4\alpha}{1 - \alpha^2}\right)^2.$$

The square of the turns ratio of the transformer is equal to

$$n^2 = \frac{b'}{b}. \quad (16)$$

It is worthwhile remembering that the primary–secondary turns ratio of the transformer, $n : 1$, is also the ratio of the voltages at its terminals. From the conservation of power, currents have the inverse ratio, and as a result, the impedance ratio at the transformer terminals is $n^2 : 1$.

The derivation of the circuit elements for the PEC case can be found in [31], [37], and [38]. The technique used is to find an approximate analytic solution to the static limit of the scattering problem, and then, to use the approximate solution as

a basis for further calculations with the variational principle [37, p. 107].

Note that for the PEC case, only two parameters B and n are sufficient to describe the junction even though in general three parameters are required for a lossless reciprocal system. The nondispersive nature of the main mode of PEC parallel-plate waveguides leads to a further symmetry in the junction that reduces the number of circuit parameters required.¹

At optical frequencies where the modes are strongly dispersive, a third circuit element is needed in order to be able to fit the elements of \mathbf{S} exactly. For that reason, we have an inductor term with a reactance X . A schematic of the circuit diagram is shown in the inset of Fig. 6(a). The PEC parallel-plate waveguide circuit is the same, with $X = 0$. The normalization that we defined in (1) leads to transmission lines with a unit characteristic impedance on both sides of the junction. From transmission line theory we get the following equalities in terms of the equivalent

¹One way to check this is by observing the failure of [37, p. 103, eq. (14)] for modes with k values that depend on b , which implies that more than two parameters are required. Conversely, numerically calculating the determinant of the impedance matrix [27, p. 216] \mathbf{Z} as suggested in [36, Ch. 3, p. 119] shows that indeed only two parameters are sufficient for the PEC case. We also verified using FDFD that (15) and (16) very precisely represent the PEC junction.

impedance looking from the left side of the circuit, Z_1 , and the equivalent admittance looking from the right side Y_2

$$-S_{11} = \frac{Z_1 - 1}{Z_1 + 1} \quad \text{and} \quad -S_{22} = \frac{1 - Y_2}{1 + Y_2} \quad (17)$$

where

$$\begin{aligned} Z_1 &= iX + \frac{1}{iB + 1/n^2} \\ Y_2 &= \left(\frac{1}{1 + iX} + iB \right) n^2 \end{aligned} \quad (18)$$

The reason why we have negative signs in front of S_{11} and S_{22} in (17) is because we defined \mathbf{S} based on the TM component of the main mode H_y . However, the norm in circuit parametrization is to use the voltage reflection and transmission coefficients, which correspond to a scattering matrix description for the transverse electric component E_x . Just as in transmission line theory where the reflection coefficient for voltage is the negative of that of the current, the same relationship also holds exactly between the reflection coefficients of E_x and H_y .

We can calculate Z_1 and Y_2 from \mathbf{S} via (17)

$$Z_1 = \frac{1 - S_{11}}{1 + S_{11}}, \quad Y_2 = \frac{1 + S_{22}}{1 - S_{22}}. \quad (19)$$

Rewriting (18) in terms of its real and imaginary parts gives

$$\begin{aligned} Z_1 &= \frac{1/n^2}{B^2 + 1/n^4} + i \left(X - \frac{B}{B^2 + 1/n^4} \right) \\ Y_2 &= \frac{n^2}{1 + X^2} + i \left(n^2 B - \frac{n^2 X}{1 + X^2} \right) \end{aligned} \quad (20)$$

Now, let the real and imaginary parts of Z_1 and Y_2 be denoted as $Z_R = \text{Re}(Z_1)$, $Z_I = \text{Im}(Z_1)$, $Y_R = \text{Re}(Y_2)$, and $Y_I = \text{Im}(Y_2)$. Using (20) we get

$$\begin{aligned} Z_1 &= Z_R + iZ_I = Z_R + i(X - Bn^2 Z_R) \\ Y_2 &= Y_R + iY_I = Y_R + i(Bn^2 - XY_R) \end{aligned}$$

and we therefore have

$$\begin{aligned} Z_I &= X - Bn^2 Z_R \\ Y_I &= Bn^2 - XY_R \end{aligned} \quad (21)$$

Inverting (21) gives

$$Bn^2 = \frac{Y_I + Y_R Z_I}{1 - Y_R Z_R} \quad \text{and} \quad X = \frac{Z_I + Z_R Y_I}{1 - Y_R Z_R}. \quad (22)$$

Once we know Bn^2 and X , we can calculate n^2 using (20) as

$$n^2 = Y_R(1 + X^2) = Z_R [1 + (Bn^2)^2]. \quad (23)$$

Using (19), (22), and (23), one can calculate the circuit parameters from S_{11} and S_{22} . In Fig. 6(a)–(c), we plotted n^2 , B , and X as a function of b'/b for the three different fixed b values of 0.1λ , 0.5λ , and 0.9λ . Due to the negligible effect of loss on junction characteristics, Figs. 3 and 6(a)–(c) carry the same information, shown in different formats. It can be seen that the PEC circuit description and the MIM circuit description lead to parameters that qualitatively have similar behaviors.

B. Simplified Model

Until now, the specific normalization we imposed on the modes (1) mapped the modal propagation of waves into equivalent transmission lines of unit characteristic impedance. In this section, we will investigate the applicability of another characteristic impedance definition for the MIM junctions. The definition we use for the characteristic impedance of an MIM waveguide of insulator thickness b is [5]

$$Z_0 = b \frac{k}{\omega \epsilon_i}. \quad (24)$$

Note that this new definition is a mere rescaling of what we mean by voltage and current of the equivalent transmission line, and such a redefinition does not change S_{11} and S_{22} but breaks the symmetry of \mathbf{S} , and therefore, $S_{12} \neq S_{21}$ [32, pp. 199–200, prb. 4.15].

From the transmission line theory, one can calculate the current reflection coefficients of the junction of two transmission lines with different characteristic impedances on the right Z_{0R} , and on the left Z_{0L} , as

$$-S_{11} = S_{22} = \frac{Z_{0R} - Z_{0L}}{Z_{0R} + Z_{0L}}. \quad (25)$$

The simplified characteristic impedance model based on (24) and (25) implies a π phase shift between S_{11} and S_{22} . We schematically plotted (25) on the Smith chart as an inset in Fig. 6(d). A comparison of the inset and Fig. 3 shows that the π phase shift condition is more and more satisfied as the waveguide dimensions are decreased to subwavelength dimensions. Fig. 6(d) also supports this observation; error in the approximate reflection coefficients of (25) decreases as the waveguide dimensions become deep subwavelength. The characteristic impedance model is valid and useful when the structure is small in comparison with the wavelength, so that the quasi-static approximation holds.

C. Interpretation of Circuit Models

In the PEC limit where there is no dispersion in the main modes, the ratio of characteristic impedances Z_{0R}/Z_{0L} , as defined in (24), limits to n^2 (16). Therefore, the transformer in the exact model can be associated with the different characteristic impedances on the two sides of the junction.

As the dimensions of the PEC parallel plate junction are scaled up, the importance of the susceptance term B increases. This is a sign of the increased influence of the higher order modes on the junction characteristics. B signifies the effect of the higher order nonpropagating modes, excited in the vicinity of the junction, on the main propagating modes. B for MIM waveguide is higher than that of PEC parallel-plate waveguide with the same insulator dimensions. We observed that using $b_s = \alpha b$, and $b'_s = \alpha b'$ as the left and right waveguide insulator thickness in (15) for $\alpha = \{1.08, 1.2, 1.4\}$ corresponding to the $b = \{0.9\lambda, 0.5\lambda, 0.1\lambda\}$ cases gave good fits to the MIM waveguide solutions plotted in Fig. 6(b). The dispersive nature of the MIM waveguide mode and the finite penetration of fields

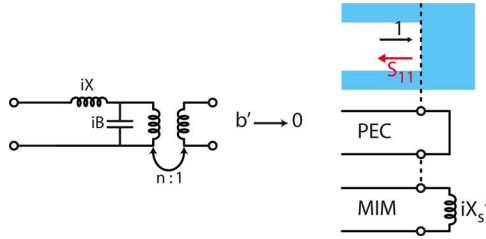


Fig. 7. Circuit models in the limit where the right waveguide width (b') goes to zero. For the PEC parallel-plate waveguide, the reflection coefficient for currents is unity. For the MIM waveguide, the reflection coefficient has a small negative phase, as is evident from Fig. 3(c). Surface reactance of metals at optical frequencies has an inductive character. Investigation of the limit $b' \rightarrow 0$ leads us to associate the inductor in our circuit model with the normalized surface reactance of the vertical metal surfaces at the MIM junction of total length $b - b'$, as shown in Fig. 1.

into the metal regions, which leads to a larger effective insulator thickness, can explain the differences in B for the MIM case [5].

The MIM junction, with its predominantly negative ϵ_m at infrared frequencies, requires an additional circuit term, an inductor with reactance X , to fully describe the junction scattering characteristics (S) using circuit terminology. We can qualitatively justify the existence of X by investigating the properties of S_{11} in the limit $b' \rightarrow 0$. We see that for the PEC case, S_{11} limits to $+1$ as highlighted in Fig. 3(c). This is in line with the fact that $B \rightarrow \infty$ and $n \rightarrow 0$ as $b' \rightarrow 0$ that leaves us with a short circuit for the PEC case (see Fig. 7). On the other hand, for the MIM case, S_{11} limits to a value with magnitude close to unity, but with a nonzero phase in the fourth quadrant of the complex plane. In order to have this behavior, the limit of X should be nonzero since both the MIM and PEC cases have the same limits for B and n . From Fig. 6(c), we can see that indeed X limits to a nonzero value as $b' \rightarrow 0$.

It is possible to associate an effective surface reactance $X_s = i\omega L_e$ with planar metal surfaces where L_e is the kinetic electronic inductance that electrons experience according to the Drude model [39].²

In Fig. 7 we schematically describe the $b' \rightarrow 0$ limit for the PEC and MIM junctions. From the circuit model, we see that

$$\begin{aligned} \text{PEC } S_{11} &= \frac{1 - 0}{1 + 0} = 1 \\ \text{MIM } S_{11} &= \frac{1 - iX'_s}{1 + iX'_s} \cong 1 - i2X'_s \end{aligned}$$

where $X'_s \ll 1$ represents the surface reactance term normalized with respect to the left waveguide's characteristic impedance. In order to have a consistent description of the junction, we should have $X = X'_s$ when $b' = 0$. This limiting behavior allows us to associate X with the effective normalized surface reactance of the perpendicular metal section of height $b - b'$ at the junction. A back-of-the-envelope calculation with $X_s \approx b\sqrt{\mu_o/\epsilon_m}$ and Z_{0L} as defined in (24) gives³

²Note that [39] uses the $e^{-i\omega t}$ convention that leads to $X_s = -i\omega L_e$.
³ $\sqrt{\mu_o/\epsilon_m}$ (where μ_o is the permeability of free space) is the surface impedance of a metallic half space which is also equal to the intrinsic impedance of the metallic medium [40].

$X'_s \approx X_s/Z_{0L} \approx \{0.082, 0.081, 0.074\}$ for the $b' \rightarrow 0$ limit of $b = \{0.9\lambda, 0.5\lambda, 0.1\lambda\}$ cases. Comparing these values to the corresponding X values in Fig. 6(c) shows that this calculation correctly predicts the order of magnitude of X'_s .

Our association of the circuit elements of the junction with physically more familiar concepts does not necessarily make any of the calculations easier. One still needs to do full-wave simulations to extract the highly coupled B , X , and n^2 parameters. Furthermore, our analysis was based on a variation of the geometry while keeping the frequency of operation fixed. Due to the highly dispersive nature of the refractive index of metals at optical frequencies, we expect that a frequency-based analysis near the resonance points of material dispersion characteristics will lead to the observation of interesting phenomena at junction geometries. Such studies can be the subject matter of future investigations. Nevertheless, we believe that the lumped circuit model at 1550 nm is valuable in developing a more intuitive understanding of modal scattering at MIM junctions, and it allows a circuit-based analysis of complex systems of guides.

V. CONCLUSION

In this paper, we investigated the properties of infrared light propagation in MIM waveguides at 1550 nm by concentrating on the symmetric junctions between waveguides of different dimensions. We applied techniques widely used in the microwave literature to characterize the MIM junctions. We used a numerical method to extract the scattering matrices of junctions of different geometries from full field solutions. We validated our characterization by designing a mode converter that concentrates light from an MIM waveguide of wavelength-sized dimension to one of subwavelength dimension with zero reflection.

We parametrized the scattering matrix of the MIM junction in terms of lumped-circuit elements to come up with a more physical picture of the junction properties. The circuit representation of the junction helps us associate the effects of geometry, material properties, and wave propagation in terms of a simple network of a capacitor, inductor, and a transformer. The scattering matrix description of junctions can be used to design optical circuitry with complex functionality using tools of circuit analysis [41], [42]. It is conceivable to build a library of junction geometries associated with their scattering matrices for different waveguides including 3-D nanometallic ones [43]. Such a library, indexed according to modal scattering and propagation properties, would be invaluable in the design of integrated optical circuits composed of many interacting components.

REFERENCES

- [1] A. A. Oliner, "Historical perspectives on microwave field theory," *IEEE Trans. Microw. Theory Tech.*, vol. MTT-32, no. 9, pp. 1022–1045, Sep. 1984.
- [2] S. A. Schelkunoff, "Forty years ago: Maxwell's theory invades engineering and grows with it," *IEEE Trans. Antennas Propag.*, vol. AP-18, no. 3, pp. 309–322, May 1970.
- [3] E. Ozbay, "Plasmonics: Merging photonics and electronics at nanoscale dimensions," *Science*, vol. 311, no. 5758, pp. 189–193, Jan. 2006.
- [4] P. J. Schuck, D. P. Fromm, A. Sundaramurthy, G. S. Kino, and W. E. Moerner, "Improving the mismatch between light and nanoscale objects with

- gold bowtie nanoantennas," *Phys. Rev. Lett.*, vol. 94, no. 1, pp. 01740-1-01740-4, Jan. 2005.
- [5] G. Veronis and S. H. Fan, "Bends and splitters in metal-dielectric-metal subwavelength plasmonic waveguides," *Appl. Phys. Lett.*, vol. 87, no. 13, pp. 131102-1-131102-3, Sep. 2005.
- [6] A. Alu and N. Engheta, "Optical nanotransmission lines: Synthesis of planar left-handed metamaterials in the infrared and visible regimes," *J. Opt. Soc. Amer. B, Opt. Phys.*, vol. 23, no. 3, pp. 571-583, Mar. 2006.
- [7] N. Engheta, "Circuits with light at nanoscales: Optical nanocircuits inspired by metamaterials," *Science*, vol. 317, no. 5845, pp. 1698-1702, 2007.
- [8] A. I. Csurgay and W. Porod, "Surface plasmon waves in nanoelectronic circuits," *Int. J. Circuit Theory Appl.*, vol. 32, no. 5, pp. 339-361, Sep./Oct. 2004.
- [9] A. Hosseini, H. Nejati, and Y. Massoud, "Design of a maximally flat optical low pass filter using plasmonic nanostrip waveguides," *Opt. Exp.*, vol. 15, no. 23, pp. 15280-15286, 2007.
- [10] A. Hosseini, H. Nejati, and Y. Massoud, "Modeling and design methodology for metal-insulator-metal plasmonic Bragg reflectors," *Opt. Exp.*, vol. 16, no. 3, pp. 1475-1480, 2008.
- [11] E. N. Economou, "Surface plasmons in thin films," *Phys. Rev.*, vol. 182, no. 2, pp. 539-554, 1969.
- [12] J. A. Dionne, L. A. Sweatlock, H. A. Atwater, and A. Polman, "Plasmon slot waveguides: Towards chip-scale propagation with subwavelength-scale localization," *Phys. Rev. B, Condens. Matter*, vol. 73, no. 3, pp. 035407-1-035407-9, Jan. 2006.
- [13] E. Feigenbaum and M. Orenstein, "Modeling of complementary (void) plasmon waveguiding," *J. Lightw. Technol.*, vol. 25, no. 9, pp. 2547-2562, Sep. 2007.
- [14] T. Takano and J. Hamasaki, "Propagating modes of a metal-clad-dielectric-slab waveguide for integrated optics," *IEEE J. Quantum Electron.*, vol. QE-8, no. 2, pp. 206-212, Feb. 1972.
- [15] R. Gordon, "Light in a subwavelength slit in a metal: Propagation and reflection," *Phys. Rev. B, Condens. Matter*, vol. 73, no. 15, pp. 153405-1-153405-3, 2006.
- [16] Z. Han and S. He, "Multimode interference effect in plasmonic subwavelength waveguides and an ultra-compact power splitter," *Opt. Commun.*, vol. 278, no. 1, pp. 199-203, Oct. 2007.
- [17] K. Tanaka and M. Tanaka, "Simulations of nanometric optical circuits based on surface plasmon polariton gap waveguide," *Appl. Phys. Lett.*, vol. 82, no. 8, pp. 1158-1160, Feb. 2003.
- [18] G. Veronis and S. H. Fan, "Theoretical investigation of compact couplers between dielectric slab waveguides and 2-D metal-dielectric-metal plasmonic waveguides," *Opt. Exp.*, vol. 15, no. 3, pp. 1211-1221, Feb. 2007.
- [19] J. R. Whinnery and H. W. Jamieson, "Equivalent circuits for discontinuities in transmission lines," in *Proc. Inst. Radio Eng.*, vol. 32, no. 2, pp. 98-114, Feb. 1944.
- [20] H. A. Jamid and S. J. AlBader, "Reflection and transmission of surface plasmon mode at a step discontinuity," *IEEE Photon. Technol. Lett.*, vol. 9, no. 2, pp. 220-222, Feb. 1997.
- [21] R. F. Oulton, D. F. P. Pile, Y. Liu, and X. Zhang, "Scattering of surface plasmon polaritons at abrupt surface interfaces: Implications for nanoscale cavities," *Phys. Rev. B, Condens. Matter*, vol. 76, no. 3, pp. 035408-1-035408-12, Jul. 2007.
- [22] P. Ginzburg and M. Orenstein, "Plasmonic transmission lines: From micro to nano scale with $\lambda/4$ impedance matching," *Opt. Exp.*, vol. 15, no. 11, pp. 6762-6767, May 2007.
- [23] J. C. Weeber, Y. Lacroute, A. Dereux, E. Devaux, T. Ebbesen, C. Girard, M. U. Gonzalez, and A. L. Baudrion, "Near-field characterization of Bragg mirrors engraved in surface plasmon waveguides," *Phys. Rev. B, Condensed Matter*, vol. 70, no. 23, pp. 235406-1-235406-12, 2004.
- [24] C. Girard, "Near fields in nanostructures," *Rep. Prog. Phys.*, vol. 68, no. 8, pp. 1883-1933, Aug. 2005.
- [25] E. D. Palik, Ed., *Handbook of Optical Constants of Solids*. New York: Academic, 1985.
- [26] H. J. Hagemann, W. Gudat, and C. Kunz, "Optical constants from the far infrared to the X-ray region: Mg, Al, Cu, Ag, Au, Bi, C, and Al_2O_3 ," *J. Opt. Soc. Amer.*, vol. 65, no. 6, pp. 742-744, Jun. 1975.
- [27] D. M. Pozar, "Microwave network analysis," in *Microwave Engineering*. Reading, MA: Addison-Wesley, 1990, pp. 220-234.
- [28] S. Ramo, J. R. Whinnery, and T. V. Duzer, *Fields and Waves in Communication Electronics*, 3rd ed. New York: Wiley, 1994.
- [29] C. Montgomery, R. Dicke, and E. Purcell, *Principles of Microwave Circuits*. London, U.K.: Peter Peregrinus, 1987 (reprint of the first publication in 1948 by the McGraw-Hill Book Company, Inc.).
- [30] P. A. Rizzi, *Microwave Engineering, Passive Circuits*. Englewood Cliffs, NJ: Prentice-Hall, 1988.
- [31] R. E. Collin, *Field Theory of Guided Waves*, 2nd ed. New York: Wiley-Interscience-IEEE, 1991, ch. 8, pp. 581-588.
- [32] R. E. Collin, *Foundations for Microwave Engineering*. New York: McGraw-Hill, 1966.
- [33] P. J. B. Clarricoats and K. R. Slinn, "Numerical solution of waveguide-discontinuity problems," *Proc. Inst. Electr. Eng.*, vol. 114, no. 7, pp. 878-887, 1967.
- [34] P. H. Smith, *Electronic Applications of the Smith Chart in Waveguide, Circuit and Component Analysis*. Malabar, FL: Robert E. Krieger, 1983.
- [35] E. L. Ginzton, "Representation and measurement of microwave circuits," in *Microwave Measurements*. New York: McGraw-Hill, 1957, pp. 313-345.
- [36] N. Marcuvitz, *Waveguide Handbook*. London, U.K.: Peter Peregrinus, 1986, ch. 5, pp. 307-309.
- [37] J. Schwinger and D. S. Saxon, *Discontinuities in Waveguides*. New York: Gordon and Breach, 1968, ch. 5, pp. 99-124.
- [38] L. Lewin, *Advanced Theory of Waveguides*. London: Iliffe, 1951, ch. 5, pp. 98-106.
- [39] T. V. Teperik, V. V. Popov, and F. J. G. de Abajo, "Total light absorption in plasmonic nanostructures," *J. Opt. A, Pure Appl. Opt.*, vol. 9, no. 9, pp. S458-S462, Sep. 2007.
- [40] S. J. Garner, D. V. Thiel, and S. G. OKeefe, "Surface impedance time domain reflectometry for the determination of ice depth," *Geophys. Res. Lett.*, vol. 24, no. 13, pp. 1599-1602, Jul. 1997.
- [41] SPICE, Wikipedia, The Free Encyclopedia [Online]. Available: <http://en.wikipedia.org/wiki/SPICE>
- [42] "S-parameter modeling using the S-element," in *HSPICE Signal Integrity User Guide, Z-2007.03* ed. Mountain View, CA: Synopsys, Mar. 2007.
- [43] G. Veronis and S. H. Fan, "Modes of subwavelength plasmonic slot waveguides," *J. Lightw. Technol.*, vol. 25, no. 9, pp. 2511-2521, Sep. 2007.



Şükrü Ekin Kocabaş (S'00) received the B.S. from Bilkent University, Ankara, Turkey, in 2002, and the M.S. degree from Stanford University, Stanford, CA, in 2004, both in electrical engineering. He is currently working toward the Ph.D. degree majoring in electrical engineering with a minor in physics.

His current research interests include modeling and fabrication of nanophotonic optoelectronic devices.



Georgios Veronis (M'99) received the B.S. degree from the National Technical University of Athens, Athens, Greece, in 1997, and the M.S. and the Ph.D. degrees from Stanford University, Stanford, CA, in 1999 and 2002, respectively, all in electrical engineering.

He was an Engineering Research Associate at Ginzton Laboratory, Stanford University. He is currently an Assistant Professor jointly at the Department of Electrical and Computer Engineering and the Center for Computation and Technology, Louisiana State University, Baton Rouge. He has authored or coauthored more than 25 refereed journal papers, and is the holder of one U.S. patent. His current research interests include the theoretical analysis of nanophotonic and plasmonic devices, and computational electromagnetics.



David A. B. Miller (M'84–SM'89–F'95) received the B.Sc. degree from St. Andrews University, St. Andrews, Scotland, and the Ph.D. degree from Heriot-Watt University, Edinburgh, Scotland, in 1979, both in physics.

From 1981 to 1996, he was with Bell Laboratories, Edinburgh, where he was the Head of the Advanced Photonics Research Department since 1987. He is currently the W. M. Keck Professor of Electrical Engineering at Stanford University, Stanford, CA, where he is also the Director of the Solid State and Photonics Laboratory and the Co-Director of the Stanford Photonics Research Center. From 1997 to 2006, he was the Director of Ginzton Laboratory, Stanford, CA. His current research interests include nanophotonic and quantum-confined optoelectronic physics and devices, and fundamentals and applications of optics in information sensing, switching, and processing. He has authored or coauthored more than 200 scientific papers, delivered more than 100 conference invited talks, and holds 62 patents.

Dr. Miller has been a board member for both the Optical Society of America (OSA) and the IEEE Lasers and Electro-Optics Society (LEOS), and in various other society and conference committees. He was the President of the IEEE LEOS in 1995. He has also been a member of boards for various photonics companies. He received the Adolph Lomb Medal and the R. W. Wood Prize from the OSA, the International Prize in Optics from the International Commission for Optics, and the IEEE Third Millennium Medal. He is a Fellow of the Royal Societies of London and Edinburgh, OSA, and the American Physical Society (APS), and holds honorary degrees from Vrije Universiteit Brussel, Brussel, Belgium, and Heriot-Watt University.



Shanhui Fan (SM'06) received the Ph.D. degree in theoretical condensed matter physics from Massachusetts Institute of Technology (MIT), Cambridge, MA, in 1997.

He was a Research Scientist at the Research Laboratory of Electronics at MIT prior to his appointment at Stanford. He is currently an Associate Professor of electrical engineering at Stanford University, Stanford, CA. His current research interests include computational and theoretical studies of solid state and photonic structures and devices, especially photonic crystals, microcavities, and nanophotonic circuits and elements. He has authored or coauthored more than 140 refereed journal articles, has given over 100 invited talks, and holds 28 US patents.

Dr. Fan is a Fellow of the Optical Society of America (OSA), and a member of the American Physical Society (APS) and The International Society for Optical Engineers (SPIE). He received a National Science Foundation Career Award in 2002, a David and Lucile Packard Fellowship in Science and Engineering in 2003, the National Academy of Sciences Award for Initiative in Research in 2007, and the Adolph Lomb medal from the OSA in 2007.